Mechanical properties of structures 3D printed with cementitious powders

Feng, P., Meng, X., Chen, J. F., & Ye, L. (2015). Mechanical properties of structures 3D printed with cementitious powders. *Construction and Building Materials*, *93*, 486-497. https://doi.org/10.1016/j.conbuildmat.2015.05.132

Published in:
Construction and Building Materials

Document Version:
Peer reviewed version

Mechanical Properties of Structures 3D Printed with Cementitious Powders

Peng FENG[1, *], Xinmiao MENG[1], Jian-Fei CHEN[2], Lieping YE[1]

1 Department of Civil Engineering, Tsinghua University, Beijing, China;

2 School of Planning, Architecture and Civil Engineering, Queen's University Belfast, Northern Ireland, UK.

***** Corresponding author:Author to whom correspondence should be addressed; Tel.: +86-10-6277-2456; E-mail: fengpeng@tsinghua.edu.cn

Abstract: The three dimensional (3D) printing technology has undergone rapid development in the last few years and it is now possible to print engineering structures. This paper presents a study of the mechanical behavior of 3D printed structures using cementitious powder. Microscopic observation reveals that the 3D printed products have a layered orthotropic microstructure, in which each layer consists of parallel strips. Compression and flexural tests were conducted to determine the mechanical properties and failure characteristics of such materials. The test results confirmed that the 3D printed structures are laminated with apparent orthotropy. Based on the experimental results, a stress-strain relationship and a failure criterion based on the maximum stress criterion for orthotropic materials are proposed for the structures of 3D printed material. Finally, a finite element analysis was conducted for a 3D printed shell structure, which shows that the printing direction has a significant influence on the load bearing capacity of the structure.

Keywords: 3D printing; cementitious material; layered structure; automatic construction; stress-strain relationship; maximum stress criterion; anisotropic structure.

1. INTRODUCTION

Recently, rapid prototyping (RP) technologies, especially three dimensional printing (3DP), have been successfully used in many areas [1-2], such as manufacturing industry [3], medical applications [4], and food preparation [5]. It is believed that RP technologies may change the whole field of production in the future [1, 6]. The 3DP technique can satisfy the requirements of diversification, industrialization, and informatization for engineered construction, making it possible to build a structure by printing. An important issue in achieving wide application of large structures is the understanding of the mechanical behavior of 3D printed products so that they can be designed to be printed in an optimal way and behave as designed.

A typical 3DP technique is an advanced RP technique using a specialized digital geometric model to construct 3D objects layer by layer using binding powder materials [1, 7]. There are many other forms of RP techniques similar to 3DP [2], including selective laser sintering (SLS) [8], fused deposition modeling (FDM) [9], digital light processing (DLP) [10], stereo lithography (SLA) [11] etc. Fig. 1 shows the relationships between these techniques. These techniques are generally all called three dimensional printing by the public for their abilities to produce 3D objects directly, but this paper focuses on a three dimensional printing technique 3DP using powder materials.

The 3D printing process used in this research is as follows [1, 7, 12]:

a) 3D digital model is first built using computer aided design (CAD) software;

b) the CAD model is then converted into standard triangulation language (STL) format;

c) the STL file is sliced into many thin digital layers;

d) each layer, containing the geometric information, is transmitted to the 3D printer in sequence;

e) the printer constructs each layer atop another according to the received data.

During printing, the nozzle of the 3DP printer sprays an adhesive agent (glue) along predetermined paths (strips) one by one in each layer. The adhesive agent binds the powder together to form a hardened solid material. When all

layers are printed one atop another, a complete 3D object is constructed.

Currently, the 3DP technique can print products using powder materials such as sand, plaster, cement, metal, and ceramic [13-15]. It is thus suitable to use liquid-particle mixed cementitious materials, such as cementitious concrete composed of cement and aggregate, to produce civil engineering projects.

The application of 3DP in engineering manufacture may shorten the development cycle, reduce the production cost, and improve productivity. When applied to civil engineering, it has the potential of reducing the number of site workers, speeding up the construction process, and reducing risks during construction. A 3DP model can also be very conveniently linked to a building information model (BIM) [16], making the whole process from design, construction, management, maintenance and even decommission digital.

The last few years have experienced rapid development of 3D printers. More and more materials can now be used in 3DP processes. The size of 3D printers has also increased rapidly, making it likely that in the near future it would be possible to build large and complex-shaped structures by printing. In 2010, Italian inventor Dini developed a large 3D printer named *D-shape* [17], which made it possible to print buildings of irregular shape. Dini is currently cooperating with Dutch architect Ruijssenaars to print a Mobius strip-like building. The construction using *D-shape* is four times as fast as the traditional means, and costs just one half as much as traditional construction. Novikov and colleagues, architects at the Institute for Advanced Architecture of Catalonia in Spain, invented a robot named *Stone Spray* which can use organic materials as the base material in 2012 [18]. This robot constructs architectural shapes by depositing a mix of soil and eco-friendly binder with the help of a jet spray system. Professor Khoshnevis at the University of Southern California in the United States has conducted a research project called “Contour Crafting” for several years [19-20]. He designed a large printer to construct concrete buildings through extruding cementitious concrete layer by layer [21], expecting to print a 2,500 square foot building in twenty hours. Meanwhile, he is attempting to apply such a technique to build extraterrestrial settlement infrastructure [22].

Buswell and his colleagues at Loughborough University in the United Kingdom have been conducting a program "3D Concrete Printing" aimed for automation in construction since 2005 [23-24]. 3D Concrete Printing is also based on the extrusion of cement mortar, but has a smaller resolution of deposition [16, 25].

Although limited research on constructing large buildings using 3D printers has been conducted, little research about the mechanical properties of 3D printed structures is available [26-28]. Since 3D printed layered cementitious materials have different microscopic structures from traditional structural materials such as concrete and steel, their mechanical behaviors may also be different. The mechanical properties of 3D printed structures are the main focus of this paper.

This paper presents a study of 3D printed products made from a powder material that has the potential for wide applications in future engineering structures. The microstructure of the material was analyzed and a series of tests was conducted for its mechanical properties. The test data provide the basis for establishing a mechanical model which is essential for advanced analysis of the behaviors of 3D printed structures.

2. 3D PRINTED SPECIMENS

2.1 Specimens

2.1.1 Material composition

In this study a plaster cementitious material was adopted to build 3D objects. The material was a mixture of plaster powder ZP150 and binder ZB60, with a volume fraction of 21.8% for the binder. The main ingredients of ZP150 were plaster, vinyl polymer and carbohydrate. The main components of the ZB60 binder were humectant and water.

2.1.2 Specimen preparation by printing

The specimens were prepared using a Spectrum Z510 3D printer produced by Z corporation using a nozzle HP 4810A 11. The printer can print products up to 356 mm (length) × 254 mm (width) × 203 mm (height).

The 3D printer consists of a feed bin and a build bin (Fig. 2) [29]. The feed bin is filled with plaster powder before printing. At the start of the 3D printing process, a roller mounted together with the print head on the gantry spreads the powder to form a base layer about one eighth of an inch thick (3.18mm) covering the base of the build bin. The print nozzle then applies the binder solution at predetermined locations, based on the digital geometric information, strip by strip until one layer is constructed. The feed bin is then raised by the thickness of one layer, while the build bin lowers by the same distance to allow the next layer to be constructed. Once the powder bed is prepared again and the nozzle is cleaned, construction of the next layer begins. The above steps are repeated until all layers are printed one atop another to complete the whole object. Fig. 2 shows a schematic view of the printing process.

2.1.3 Coordinate system

To study the detailed structure of 3D printed components, a coordinate system is defined in reference to the actual printing procedure (Fig. 3). The X axis is defined as the strip direction in which the nozzle moves when it sprays the binder along the gantry, so all strips are parallel to the X axis. The Y axis is perpendicular to the strip (X) direction in the plane of a printing layer, that is, the direction in which the nozzle moves from one strip to the next. The Z axis is the vertical direction perpendicular to the printing layer (Fig. 3). The process of 3DP can then be described as follows using the coordinate system:

(1) The nozzle moves along a predetermined line parallel to the X axis and sprays the binder at a controlled rate. The travel distance and area of spray are determined by the digital geometric data of object;

(2) After completing one strip, the nozzle moves a distance equal to the width of a strip in the Y direction, and then starts to print the next strip;

(3) Once one layer is completed, the base of the build bin is lowered by a distance equal to the thickness of one layer in the Z direction. Then the powder of next layer is spread by the roller, while the nozzle is cleaned at the same time, before the printer starts to print the next layer.

Fig. 3 shows the process of printing a cubic specimen. The nozzle sprays binder from A_1 to B_1, and then moves to B_2 and further to A_2 without spraying. It sprays again when moves from A_2 to B_2 to complete the second strip. This process is repeated until the nozzle sprays from A_n to B_n to finish one layer, and the layering process is repeated until the cube is printed.

When printing cubic specimens specific to the following tests, the nozzle moved in the X direction at a high speed of about 460 mm per second when spraying, which was much faster than that in Y direction. Clearly, the time between printing two adjacent strips was much shorter than that between adjacent layers. This difference in time intervals between printing adjacent strips and layers may have a significant influence on the mechanical properties of 3D printed specimens.

Once printing was finished, the base of the build bin was raised to remove the printed products from the powder bed. The extra powder that still covered the objects was first brushed off and then sucked up with vacuuming. Finally, to accelerate solidification and accordingly increase strength, the freshly printed objects were placed in an oven at 60 ^{o}C for three hours so that they were completely dry. The density of the hardened specimens was about 1.34g/cm^3. Fig. 4 shows the actual procedure of printing specimens.

2.2 Microstructure of printed objects

The surface structure of a printed 50 mm cubic specimen was inspected by using both a 3D high-depth stereo microscope and naked-eyes recorded using a high resolution digital camera. Fig. 5 shows typical photographs, from which the characteristics of the 3D specimen can be summarized as follows:

(1) Layered microstructure. The 3D printed sample with cementitious powder material has a clearly layered microstructure. Many parallel lines can be seen clearly in the XZ plane. The layered printing structure is also evident in the particle configuration in the YZ plane, but it is not as apparent as that in the XZ plane.

(2) Striped structure in each layer. Each layer is composed of many strips, as clearly shown in the XY plane which

is consistent with the printing process.

(3) Orthotropy. The XZ face is the roughest of the three faces, the YZ face is smoother, with the XY face in between. Based on the printing procedure (Fig. 3) and observations of the surface structure, it is clear that such a material is orthotropic.

3. MECHANICAL TESTS

Compression tests of cubes and flexural tests of small beams were conducted to determine the basic mechanical properties of the 3D printed material, including strength, elastic modulus and Poisson's ratio. Failure characteristics of the tested specimens are also described below.

3.1 Compression test

3.1.1 Specimens

Two batches of printed cubes, one with side length of 70.7 mm and the other with 50 mm were produced and tested for the compression behavior. Each batch was printed in a single printing cycle. Both batches had the same ingredients and were produced using the same printing method with a layer thickness of 0.0875 mm.

The batch of the larger specimens was divided into two groups of three specimens each. The specimens in the first group, designated CZ-B1 to CZ-B3, were loaded in the Z direction. Those in the second group, designated CX-B4 to CX-B6, were loaded in the X direction. In the specimen designations, the first letter C represents compression test, the second letter represents the loading direction (either X or Z), followed by the specimen size (B for the bigger specimens and S for the smaller specimens). Two pairs of foil strain gauges, each pair consisting of one horizontal and one vertical gauge, were bonded at the center of two opposite faces of each specimen. The gauges had an active grid length of 3 mm and an electrical resistance of 120 Ω. The specimens were about one month old at the time of test.

The batch of smaller specimens was divided into three groups, with three specimens in each. They were loaded respectively in X, Y and Z directions. Based on the above rules, the specimens in the three groups were designated CX1 to CX3, from CY1 to CX3 and from CZ1 to CZ3 respectively. Four pairs (horizontal and vertical) of foil strain gauges were attached at the centre of the four vertical faces for each specimen.

3.1.2 Test

The compression test followed the test procedure prescribed in the Chinese "*Standard for test method of mechanical properties on ordinary concrete"* (GB/T50081-2002) [30]. The loading rate ranged between 0.1 kN/s and 0.3 kN/s. The compression strength was obtained from the maximum load divided by the face area of the cubes. The modulus of elasticity and Poisson's ratio were calculated from the initial linear branch of the stress-strain relationship curve. The measurement of modulus and Poisson's ratio using cube specimens is less accurate compared with cylindrical specimens due to frictional constraints at the contact surfaces, but the cylindrical specimen was not used because of limitations of the printing capacity of the 3D printer: it does not print cylindrical specimens well, especially when printing vertically along the longitudinal direction. Each specimen was pre-loaded twice to a stress of 0.5MPa, before loaded to failure. In order to minimize loading eccentricity, the position of a specimen was adjusted after each preloading based on the differences between strain readings from gauges on the opposite faces.

3.1.3 Failure mode and other observations

When loaded in the Z direction, both large and small cubes have similar phenomena. At the beginning of loading, the deformation was small in these specimens. When approaching to the maximum load, diagonal cracks occurred in the YZ plane and they developed quickly. When the ultimate load was reached, the specimens exhibited diagonal failure with two sets of triangular cracks intersecting near the centre to form an hourglass shape on the two opposite sides in the YZ plane as red dashed lines indicated in Figs. 6 and 7. Some local damage following the printed strips

appeared in the contact region between the upper loading platen and the corner of the specimen as shown in Fig. 7. When loaded in the X direction, the behavior of both large and small cubes was similar to that under Z-direction compression. The only difference is that the hourglass shaped cracks were now formed on the opposite faces in the XZ plane (Figs 6 and 8), instead of the YZ plane when under Z-direction compression. Probably due to printing defects, the large specimen CX-B6 failed in a different mode, namely layer splitting.

Under Y-direction compression for the small cubes, the behavior was similar initially but the diagonal cracks in the YZ plane were finer and developed much slower (Fig. 9). If the specimens were continuously loaded post peak, the above-described hourglass cracks on two opposite sides (in the YZ plane) as in Fig. 6 were still developed.

3.1.4 Results and analysis

The compressive cube strength and the elastic modulus of the specimens are listed in Table 1. The Poisson's ratio is given in Table 2. The elastic modulus and the Poisson's ratio of the specimens were determined from the initial linear segment of the experimental stress-strain curve. The elastic modulus was the slope of the linear segment of vertical stress-strain curve, while the Poisson's ratio was the negative ratio of the horizontal to the vertical strain. Table 1 shows that the modulus in the X direction is the highest, and that in the Z direction is the lowest, with that in the Y direction in between.

The test results show that the compression strength in the X direction is higher than that in both Y and Z directions. According to the printing process, the specimens can be seen as many thin strips overlaying one after another (Fig. 10). The printing speed is high in the X direction, and the time of printing adjacent strips (Y direction) is much shorter than that of printing adjacent layers (Z direction). The bond between two parts of the material appears to be higher when they are printed within a shorter period of time, resulting in a higher strength inside a continuous strip than that between strips, which is in turn higher than that that between layers. When loaded in the X direction, the cracks pass through inter-layer interfaces (vertical component of crack path) and strips (horizontal component of

crack path), giving the highest strength in the three directions as the bond strength within strips is the highest. When loaded in the Y direction, the cracks pass through the inter-layer interfaces (vertical) and inter-strip interfaces (horizontal). When loaded in the Z direction, the cracks pass through the inter-strip interfaces (vertical) and inter-layer interfaces (horizontal). As shown in Fig. 6, the crack faces have an angle higher than 45 degrees (to horizontal) so that the vertical path is slightly longer than the horizontal path, giving a higher strength in the Z direction because the inter-strip strength is higher than the inter-layer strength.

The tensile behavior in the three directions may be deduced following the above analyses. When loaded in the X direction, tensile cracks would most likely appear in the YZ plane which would be dependent on the bond strength within the strips. Similarly, when loaded in the Y direction, cracks would appear in the XZ plane which would be dependent on the inter-strip bond strength and when loaded in the Z direction, cracks would appear in the XY plane which depends on the inter-layer bond strength. Therefore, the tensile strength would be the highest in the X direction and the lowest in the Z direction, with the Y direction in between.

The test results show that the smaller specimens have higher compression strength and elastic modulus than those of the larger ones. There might be two mainly causes for this phenomenon: one is the curing time. The curing time was about one month for the larger samples but about 6 months for the smaller ones; the other is the size effect. It takes longer to print larger specimens and consequently the stability of 3D printing process may reduce as the nozzle may be slightly blocked which leads to poorer bond. Additionally, the larger specimens may also have more defects statistically which also leads to lower strength and modulus. However, the failure process and failure modes had little difference between the larger and smaller specimens.

There are several “outliers” in the test data, such as the Poisson’s ratio of CZ-B3 and the compression strength of CX-B6. They are likely due to defects arisen from the printing process, such as inconsistence in the content of binder in different parts of a specimen.

From the above analysis, it can be concluded that both the size of specimens and loading direction have an effect on the mechanical properties including strength, elastic modulus and Poisson's ratio. The 3D printed materials are apparently anisotropic. The printing procedure ensures that such material has an orthotropic structure.

3.2 Flexural test

3.2.1 Specimens

The flexural tests were conducted with 40mm × 40mm × 160mm specimens. The specimens were divided into two groups of three, one loaded in the Z direction (Fig. 11a) to study the tensile properties within strips. The other loaded in the X direction to study the interlayer bond properties (Fig. 11b). Each specimen was assigned a unique designation, starting with F (for flexural), followed by either Z (for Z-direction loading) or X (for X-direction loading), then followed by "-An" with n being the specimen number (1 to 6).

3.2.2 Test

The flexural tests were conducted following the Chinese national standard GB/T 17671-1999 for testing strength of cements [31]. A typical test setup is shown in Fig.12. The applied loading rate was about 50N/s. The flexural strength was determined based on the linear elastic analysis using the first crack load.

The deformation was not obvious until the maximum load was attained. Once the maximum load was reached, the bottom of the specimen was cracked suddenly leading to a sharp drop of the load and the test was stopped. The failure modes were different for the two groups of specimens loaded in different directions shown in Fig. 13, in two aspects:

(1) The development of cracks was different. When loaded in the X direction, the cracks propagated suddenly through almost the whole section once it cracked. However, when loaded in the Z direction, the crack developed slower than that in the X direction, with the crack length less than half of the cross-section depth correspondingly.

(2) The position of cracks was also different. When loaded in the Z direction, the cracks appeared at the middle of the specimen. But when loaded in the X direction, the cracks deviated slightly from the middle to the part of the specimen printed late due to non-uniformity caused by the printing process (Fig. 13b) which took over ten hours for each specimen.

3.2.3 Results and analysis

The peak loads from the flexural tests were used to obtain the flexural strength R_f according to:

$$R_f = \frac{1.5F_f L}{b^3} \quad (1)$$

where F_f is the maximum load, L is the distance between two supports, b is the side length of a square cross section.

The calculated flexural strengths are shown in Table 3. It can be seen that when loaded in the Z direction, the flexural strength is one order higher than that loaded in the X direction. As mentioned above, the bond strength inside a strip is higher than that between layers. When loaded in the Z direction, the flexural strength depends on the bond strength inside a strip, in contrast, it relies on the interlayer bond strength when loaded in the X direction.

3.3 Compression test after relevant flexural test

3.3.1 Specimen

The flexural test specimens were continuously flexed after reaching the peak load until a specimen was separated into two halves completely. The two halves of each specimen after each flexural test were used to conduct compression test. When loaded in the Z direction during flexural test, the crack was located in the middle of the beam so the two halves were almost the same size. When loaded in the X direction, the crack was slightly away from the middle, but the tests still satisfied the size requirement that there is at least 10mm outside the loading area in the longitudinal direction of the specimen (Fig. 14).

3.3.2 Test

The compression test was conducted following the Chinese standard "*Method of testing cements-Determination of strength"* (GB/T 17671-1999) [31]. The loading area was 40mm × 40mm with an edge at least 10 mm wide outside the loading area in the longitudinal direction as shown in Fig. 14. The loading rate was about 1.2 kN/s. The compression strength is calculated from the maximum load divided by the compression area.

When loaded in the Z direction, there was little deformation at first. As the load increased, gradual local crushing occurred in the loaded area. When approaching the ultimate load, diagonal cracks appeared, beginning from the edges of the loaded zone and propagating diagonally in the XZ plane (Fig. 15a). However, when loaded in the X direction, there was little noticeable compression deformation in the loaded area. The failure mechanism was mostly interlayer shear failure resulting in the loaded portion pushed out of the specimen, with short diagonal cracks occurred only in a few specimens (Fig. 15b).

3.3.3 Results and analysis

The compression test results on the half beams are shown in Table 4. Note that each flexural specimen was broken into two halves, giving two compression test specimens. Table 4 shows that the specimens had higher strength when loaded in the Z direction than that in the X direction, which is completely opposite to the compression strength test result of cubic specimens. This is mainly because the two tests were conducted following different methods, leading to the different failure modes. In the compression test of half beams, the specimen was partially loaded (Fig. 16). This led to interlayer shear failure along the boundaries of the loaded area when loaded in the X direction. The failure load mainly depended on the interlayer shear strength, which in turn relied on the interlayer bond strength, the lowest bond strength in three directions. Therefore, the failure load in the X direction is lower than that in the Z direction. However, in the compression test of cubes, the specimens were loaded uniformly, leading to higher compression strength in the X direction without shear failure (Fig. 16).

Table 4 also shows that the test results are stable and consistent when loaded in the Z direction, but have very high

variability when loaded in the X direction. This may be that the bond of inter-layer interface varied a lot more than that of the inter-strip bond within a layer and the bond within a strip. Another major contributing factor may be the variation of printing quality. The specimen was 160 mm long in the Z direction for the flexural specimens so it took over ten hours to print one specimen. At the beginning, the printing quality was very good, and the binder content was stable. However, there might be built-ups in the nozzle as time increases, leading to reduced printing quality as a result of less denser printed material and poorer interlayer bond. This can explain the lower compression strength of the later printed half of the flexural specimens when loaded in the X direction.

4. MECHANICAL MODELS

4.1 Stress-strain relationship

The cube test results were analyzed for developing compressive stress-strain relationships in different directions. Fig. 17 shows that each curve is almost linear initially but softens gradually as the stress increases. No apparent yield or horizontal segment is evident. Once it reaches the maximum load, it fails in a brittle manner. No descending branch was obtained because the tests were conducted under load control.

Based on the above observations, a parabolic curve may be used to describe the stress-strain relationship:

$$\sigma = \frac{f_0 - E_0\varepsilon_u}{\varepsilon_u^2}\varepsilon^2 + E_0\varepsilon \tag{2}$$

where σ is stress under uniaxial compression; f_0 is the maximum stress; E_0 is the initial elastic modulus; ε is the strain under uniaxial compression; and ε_u is the ultimate strain, $\varepsilon_u = 2f_0/E_0$ if ε_u is greater than $2f_0/E_0$. Although the frictional restraints of the loading platens cannot be avoided and enhance the compressive strength in the cube test, the cube strength is used as the reference uniaxial compressive strength. The average values of f_0, E_0 and ε_u for the smaller specimen group which was tested in all three directions are shown in Table 5. If they are used in Eq. (2), the results are in close agreement with the test results (Fig. 17).

In tension, the 3D printed specimens may be assumed linear-elastic brittle, similar to what appeared in the flexural tests. All specimens failed on the tension side in a brittle fashion. The flexural strength is used as the equivalent uniaxial tensile strength in this study before more test data become available.

4.2 Failure criterion

The above test results have shown remarkable orthotropy of 3D printed cementitious products. A failure criterion suitable for orthotropic materials is required for failure analysis of such structures. Several failure criteria are available for orthotropic materials, such as Hoffman's (1967) or Tsai-Wu's (1971) criterion. Since only unaxial tests were conducted in this study, the maximum stress criterion may be suitable. Hoffman criterion can be defined by unaxial test data, but there are no biaxial test data to verify its validity. Tsai-Wu's criterion requires biaxial tests to determine the parameters. Therefore, the maximum stress criterion [32] is used here to describe the mechanical behavior of the 3D printed specimens. In the maximum stress criterion, the stresses in the principal material coordinates must be all smaller than the respective strengths to avoid fracture. It is expressed as:

for tensile stresses,

$$\sigma_1 < X_t, \ \sigma_2 < Y_t, \ \sigma_3 < Z_t \tag{3}$$

and for compressive stresses,

$$\sigma_1 > X_c, \ \sigma_2 > Y_c, \ \sigma_3 > Z_c \tag{4}$$

and for shear stresses,

$$|\sigma_{12}| < S_{12}, \ |\sigma_{23}| < S_{23}, \ |\sigma_{31}| < S_{31} \tag{5}$$

where σ_i（i=1, 2, 3）is the stress in the principal material coordinate (i.e. the coordinate system defined for the 3D printing, where directions 1, 2 and 3 correspond to the X-, Y- and Z- directions respectively in this study, σ_{12}, σ_{23}, σ_{31} are shear stresses in the respective planes of the principal material coordinates, X_i, Y_i, Z_i (i=t, c) are the maximum allowable stresses in different directions in tension (i=t) and compression (i=c), and S_{12}, S_{23}, S_{31} are the

maximum allowable shear stresses in the different planes. X_i, Y_i, Z_i (i=t, c) and S_{12}, S_{23}, S_{31} can be determined by nine simple uniaxial tests, including tension tests and compression tests in three directions and shear tests in three planes.

The compression strengths of the smaller specimens are used here as an example for the maximum stress criterion, because the tests of the smaller cubes were more complete with data from loading in all three directions. To determine the shear strength, simple direct double shear test was conducted for short rectangular beams as shown in Fig. 18 following the standard test for concrete [33]. Test data were validated only when the failure occurred along the preferred failure plane. The resulting shear strengths were 0.628 MPa in the XY plane, 4.63 MPa in the YZ plane, and 1.264 MPa in the XZ plane. The flexural strength in the X and Z directions may be treated approximately as the direct tensile strengths. The Y direction tensile strength is not directly available in this study. As mentioned early, the tensile strength is greater in the X direction than that in the Y direction which is in turn greater than that in the Z direction, so the tensile strength in the Y direction was assumed to be 1MPa in the example here. The values of the maximum allowable strengths in the maximum stress criterion are summarized as follows:

$$X_t = 4.12 \text{ MPa}, X_c = -16.8 \text{ MPa}, Y_t = 1\text{MPa}, Y_c = -11.6 \text{ MPa}, Z_t = 0.365\text{MPa}, Z_c = -13.2\text{MPa}$$

$$S_{12} = 0.628\text{MPa}, S_{23} = 4.632\text{MPa}, S_{31} = 1.264\text{MPa}$$

4.3 Application of the constitutive model

For constructing practical engineering structures, either 3D printing prefabrication or in-situ 3D printing construction may be adopted based on various considerations. For 3D printing prefabrication, it would be convenient if the printing process is vertical, i.e. the Z direction is perpendicular to the printed layers. However, loading in a given printing direction is not necessarily always ideal, so the loading direction can be controlled by printing elements in different orientations (i.e. printing a column "laying down") and then positioning it vertically

in the structure. Because of the orthotropic nature of the 3D printed structures, the relationship between loading direction and printing direction can be important: a careful selection of these angles based on structural analysis may significantly enhance the behavior of the structure. For in-situ 3D printing construction, the printing direction is already determined by the printing principle, so it is necessary to optimize the structural design based on the mechanical properties to ensure safety and economy. The relationship between mechanical behavior and printing directions is evaluated through a simple example here.

A finite element analysis (FEA) of an example 100mm thick arch structure was conducted using the maximum stress criterion with the constants listed above. The FEA was conducted using MSC.Marc 2007 to assess the influence of printing direction on the structural performance. The example structure as shown in Fig. 19a is 1 m in height, 1 m in width and 3 m in length. It was modeled using the 8-node hexahedral solid element (7 # solid), with the above properties for the orthotropic material constitutive law. The total number of elements was 1,560 and the size of elements was about 33mm. The structure was analyzed under dead weight and a vertical surface (not necessarily uniform) load on the top platform. The boundaries at the supports were fixed (i.e. restrained in all directions). In the model, the dead weight was applied to all elements as the initial condition, and the surface load was applied through displacement control to the nodes of the loaded surface. The progressive failure analysis option was turned on (with a residual stiffness coefficient of 0.01) to achieve gradual degradation of the elastic modulus during the failure process. The loading process was conducted using the full Newton-Raphson method. The element coordinate system was changed in each analysis to simulate different printing direction of the structure as shown in Figs 19(b) (c) (d).

Figs 19(b) (c) (d) also show the failure locations, which are similar for all cases. Fig. 20 shows that when loaded in the X direction, the maximum loading capacity of the structure is the lowest with an average surface load of 24.5kN/m^2; when loaded in Z direction, it is 33.3kN/m^2; when loaded in Y direction, the capacity is highest at

69.4kN/m^2. The results show that the printing direction has a very significant effect on the overall load bearing capacity of the structure. This confirms the importance of choosing suitable printing direction in the case of 3D prefabrication.

4.4 Potential developments and applications of 3DP

The test data indicate that the structures 3D printed with cementitious plaster powders in this study are not suitable for structural members because of their brittleness and low strength. However, they may be used and indeed have found applications for non-structural components such as printing building decorations, formworks for nonlinear architectural features. Nevertheless, the layered microscopic characteristics and orthotropic mechanical behavior are representative of 3D printed structures with cementitious powders. Further study should been conducted to use 3D printers using cement or other materials rather than plaster powders to produce high-strength structures. It would also be desirable to either add reinforcements during the printing process or use the 3D printed material in combination of other materials such as steel and Fiber Reinforced Polymer (FRP) composites, the latter has found wide applications in strengthening concrete structures [34]. Preliminary study has shown that the structural capacity and ductility can be significantly improved for 3D printed columns and beams when strengthened with FRP.

The 3D printer used in this study is an industrial grade machine suitable for printing small objects precisely. Consequently, the cost for printing these specimens was high (about 0.50 USD per cubic centimeter. However, with the development of large 3D printers and suitable materials specifically designed for printing structures such as buildings, there is no doubt that the cost will decline dramatically.

In smmary, the 3D printing technology has the potential to provide an effective method to achieve low-cost, high-efficient automatic construction with reduced waste, labor cost and construction risks. It can significantly speed up the construction process.

5. CONCLUSIONS

This paper has presented a study on the characteristics of a 3D printed layered cementitious material, through microscopic observation, mechanical test of cubes and small beams, and FE modelling on the effect of construction process on the structural behavior. The basic mechanical parameters and failure characteristics in different directions were obtained through compression tests of cubes and flexural tests of small-scale beams. In addition, a model for the stress-strain relationship had been proposed based on the uniaxial test stress-strain curves under compression. On the basis of the test data, parameters for the maximum stress criterion were also defined for the 3D printed orthotropic cementitious material. These relationships were deployed in an FE analysis of a 3D printed arch structure to investigate the effect of printing direction on the load carrying capacity. The main conclusions are as follows:

(1) The layer-atop-layer printing process results in the printed material of layered microscopic structure with each layer further consisting of bonded strips, leading to an apparent orthotropic behavior;

(2) All 3D printed cubes had similar failure mode with hourglass-shaped cracking on opposite sides when loaded in the X-, Y- and Z- directions, but the compression strength and elastic modulus are the highest when loaded in the X-direction (printer head travel direction);

(3) Based on the uniaxial compression test results, the stress-strain relationship of the 3D printed cementitious material may be described by a quadratic model;

(4) Based on the maximum stress criterion adapted for the 3D printed orthotropic material, a finite element analysis of a thin shell structure was conducted. The results have shown that the printing direction has a significant effect on the load bearing capacity of the structure.

ACKNOWLEDGMENTS

The authors acknowledge funding support from the National Natural Science Foundation of China (No. 51278276), the National Basic Research Program of China (973 Program, No. 2012CB026200). The first author also acknowledges funding support from the Beijing Higher Education Young Elite Teacher Project (YETP0078) and Tsinghua University Initiative Scientific Research Program (No.20111081015).

REFERENCES

[1] Lipson H, Kurman M. Fabricated: The new world of 3D printing. John Wiley & Sons, 2013.

[2] Dimitrov D, Schreve K, De Beer N. Advances in three dimensional printing – state of the art and future perspectives. Rapid Prototyping Journal, 2006; 12(3): 136-147.

[3] Berman B. 3-D printing: The new industrial revolution. Business horizons, 2012; 55(2): 155-162.

[4] Lam CXF, Mo XM, Teoh SH, Hutmacher DW. Scaffold development using 3D printing with a starch-based polymer. Materials Science and Engineering: C, 2002; 20(1), 49-56.

[5] Wegrzyn TF, Golding M, Archer RH. Food layered manufacture: A new process for constructing solid foods. Trends in Food Science & Technology, 2012; 27(2), 66-72.

[6] Yan X, Gu P. A review of rapid prototyping technologies and systems. Computer-Aided Design, 1996; 28(4): 307-318.

[7] Cima MJ, Haggerty JS, Sachs EM, Williams PA. Three-dimensional printing techniques: U.S. Patent 5,204,055. 1993-4-20

[8] Gibson I, Shi D. Material properties and fabrication parameters in selective laser sintering process. Rapid Prototyping Journal, 1997; 3(4): 129-136.

[9] Kulkarni P, Dutta D. Deposition strategies and resulting part stiffnesses in fused deposition modeling. Journal of manufacturing science and engineering, 1999; 121(1): 93-103.

[10] Hornbeck LJ. Digital light processing update: status and future applications. Electronic Imaging'99. International Society for Optics and Photonics, 1999: 158-170.

[11] Ikuta K, Hirowatari K, Ogata T. Three dimensional micro integrated fluid systems (MIFS) fabricated by stereo lithography. Micro Electro Mechanical Systems, 1994, MEMS'94, Proceedings, IEEE Workshop on. IEEE, 1994: 1-6.

[12] Jurrens KK. Standards for the rapid prototyping industry. Rapid Prototyping Journal, 1999; 5(4): 169-178.

[13] Utela B, Storti D, Anderson R, Ganter M. A review of process development steps for new material systems in three dimensional printing (3DP). Journal of Manufacturing Processes, 2008; 10(2): 96-104.

[14] Singh R. An overview of three dimensional printing for casting applications. International Journal of Precision Technology, 2011; 2(1): 93-116.

[15] Singh R. Three dimensional printing for casting applications: A state of art review and future perspectives. Advanced Materials Research, 2010; 83: 342-349.

[16] Lim S, Buswell RA, Le TT, Austin SA, Gibb AG, Thorpe T. Developments in construction-scale additive manufacturing processes. Automation in construction, 2012; 21: 262-268.

[17] D-Shape. http://www.d-shape.com.

[18] Stone spray project. http://www.stonespray.com/

[19] Contour Crafting. http://www.contourcrafting.org/

[20] Khoshnevis B. Automated construction by contour crafting—related robotics and information technologies. Automation in construction, 2004; 13(1): 5-19.

[21] Khoshnevis B, Hwang D, Yao K, Yeh Z. Mega-scale fabrication by contour crafting. International Journal of Industrial and Systems Engineering, 2006; 1(3): 301-320.

[22] Khoshnevis B, Thangavelu M, Yuan X, Zhang J. Advances in contour crafting technology for extraterrestrial

settlement infrastructure buildup. AIAA SPACE 2013 Conference and Exposition 2013.

[23] 3D Concrete Printing. http://www.buildfreeform.com/

[24] Buswell RA, Soar RC, Pendlebury M, Gibb AG. Investigation of the potential for applying freeform processes to construction. 2005. https://dspace.lboro.ac.uk/2134/10144

[25] Buswell RA, Soar RC, Gibb AG, Thorpe A. Freeform construction: mega-scale rapid manufacturing for construction. Automation in Construction, 2007; 16(2): 224-231.

[26] Giordano RA, Wu BM, Borland SW, Cima LG, Sachs EM, Cima MJ. Mechanical properties of dense polylactic acid structures fabricated by three dimensional printing. Journal of Biomaterials Science, Polymer Edition, 1997; 8(1): 63-75.

[27] Ahn SH, Montero M, Odell D, Roundy S, Wright PK. Anisotropic material properties of fused deposition modeling ABS. Rapid Prototyping Journal, 2002; 8(4): 248-257.

[28] Lee CS, Kim SG, Kim HJ, Ahn SH. Measurement of anisotropic compressive strength of rapid prototyping parts. Journal of Materials Processing Technology, 2007; 187: 627-630.

[29] Spectrum Z510/DesignmateTM CX 3D Printer, User Manual Rev X, Z Corporation 2006.

[30] GB/T50081-2002 Standard for test method of mechanical properties on ordinary concrete. Beijing, 2003.

[31] GB/T 17671-1999 Method of testing cements-Determination of strength. Beijing, 1999.

[32] Jones RM. Mechanics of composite materials. CRC press, 1998.

[33] CECS13:89 Test methods used for steel fiber reinforced concrete. Beijing, 1996.

[34] Teng JG, Chen JF. Mechanics of debonding in FRP-plated RC beams. Proceedings of the Institution of Civil Engineers – Structures and Buildings, 2009; 62(5): 335-345.

FIGURE CAPTIONS

direction and failure position, (c) loaded in Y direction and failure position and (d) loaded in Z direction and failure position.

Fig. 20 Load-displacement curves of the structure when constructed in different directions

Table 1 Compressive strength and elastic modulus of cubic specimens

	Specimen	Compressive strength (MPa)			Elastic modulus (GPa)		
		Value	Average	Standard deviation	Value	Average	Standard deviation
70.7 mm specimens	CX-B4	11.5	11.2	1.92	3.5	3.6	0.26
	CX-B5	10.9			3.9		
	CX-B6*	7.92			3.4		
	CZ-B1	7.89	7.23	0.64	1.8	1.9	0.31
	CZ-B2	7.18			2.2		
	CZ-B3	6.61			1.6		
50 mm specimens	CX1	16.5	16.8	0.38	6.4	7.1	0.61
	CX2	16.6			7.2		
	CX3	17.2			7.6		
	CY1	13.4	11.6	1.63	7.0	5.8	1.15
	CY2	10.2			4.7		
	CY3	11.3			5.7		
	CZ1	12.1	13.2	1.04	4.8	4.9	0.36
	CZ2	13.9			4.6		
	CZ3	13.9			5.3		

* excluded as it had printing defects.

Table 2 Poisson's ratio of cubic specimens

	Specimen	Poisson's ratio	Average	Poisson's ratio	Average
70.7 mm specimens		γ_{ZY}		γ_{ZX}	
	CZ-B1	0.138			
	CZ-B2	0.129	0.166	undetermined	
	CZ-B3	0.232			
		γ_{XY}		γ_{XZ}	
	CX-B4	0.261			
	CX-B5	0.232	0.270	undetermined	
	CX-B6	0.318			
50 mm specimens		γ_{XY}		γ_{XZ}	
	CX1	0.307		0.267	
	CX2	0.302	0.285	0.303	0.311
	CX3	0.275		0.362	
		γ_{YX}		γ_{YZ}	
	CY1	0.302		0.232	
	CY2	0.241	0.250	0.390	0.306
	CY3	0.201		0.325	
		γ_{ZX}		γ_{ZY}	
	CZ1	0.166		0.133	
	CZ2	0.147	0.147	0.168	0.157
	CZ3	0.127		0.169	

Table 3 Flexural strength

Specimen	Flexural strength (MPa)	Average (MPa)	Standard deviation (MPa)
FZ-A1	4.14		
FZ-A2	4.30	4.12	0.19
FZ-A3	3.93		
FX-A4	0.326		
FX-A5	0.404	0.365	0.06
FX-A6	0.155*		

*: Data excluded as it lies out of ±10% of the average, reported average is that of the remaining two following the testing standard [31].

Table 4 Compressive strength of the half beams

Specimen	Compressive strength (MPa)		Average (MPa)	Standard deviation(MPa)
CZ-A1	7.84	7.88		
CZ-A2	7.91	7.81	7.79	0.16
CZ-A3	7.83	7.48		
CX-A4	5.38	2.46		
CX-A5	6.38	3.36	N/A*	N/A*
CX-A6	5.19	1.87		

* Scatters too large so not processed.

Table 5 Values of parameters for the proposed stress-strain curve

	Loading direction	f_0 (MPa)	E_0 (GPa)	ε_u ($\times 10^{-6}$)
50mm specimens	X	16.8	7.1	3100
	Y	11.6	5.8	3000
	Z	13.2	4.9	3800

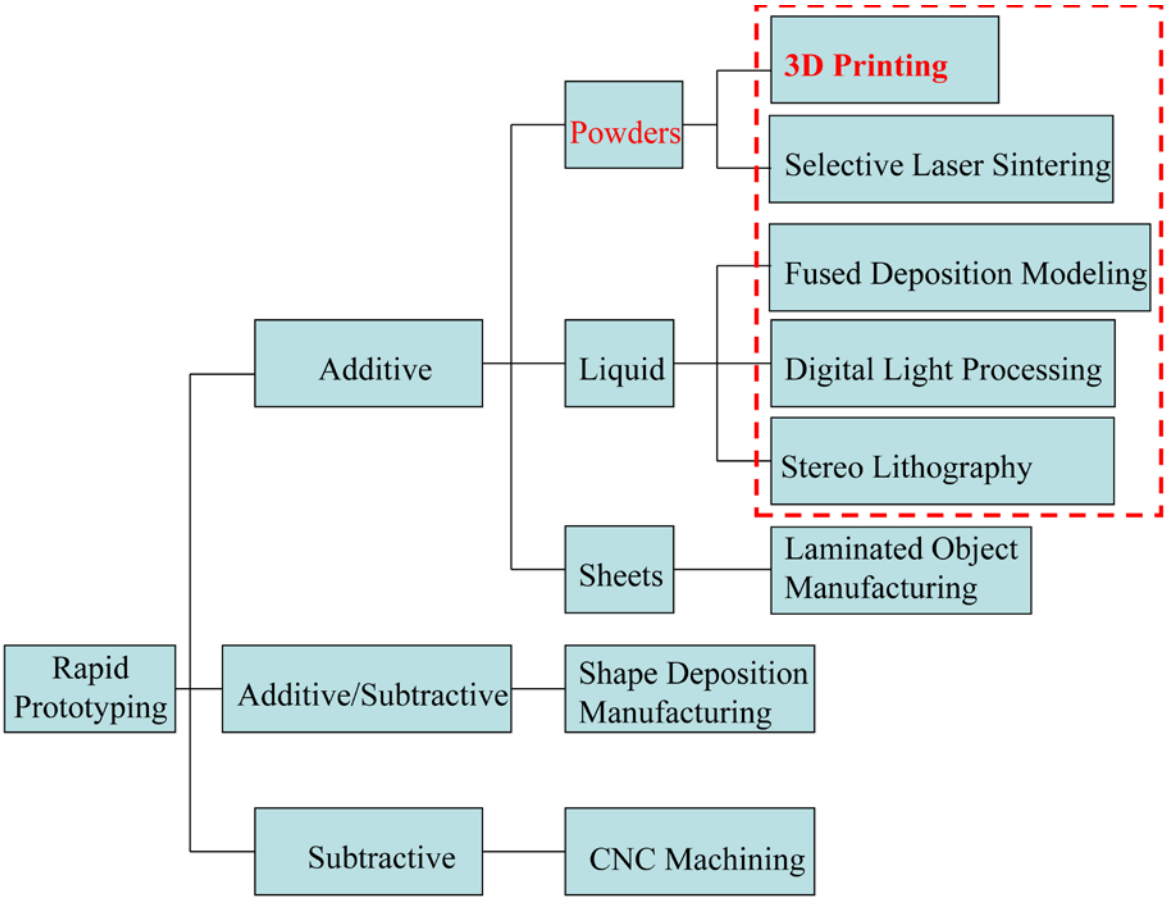

Fig. 1 Classification of RP technologies

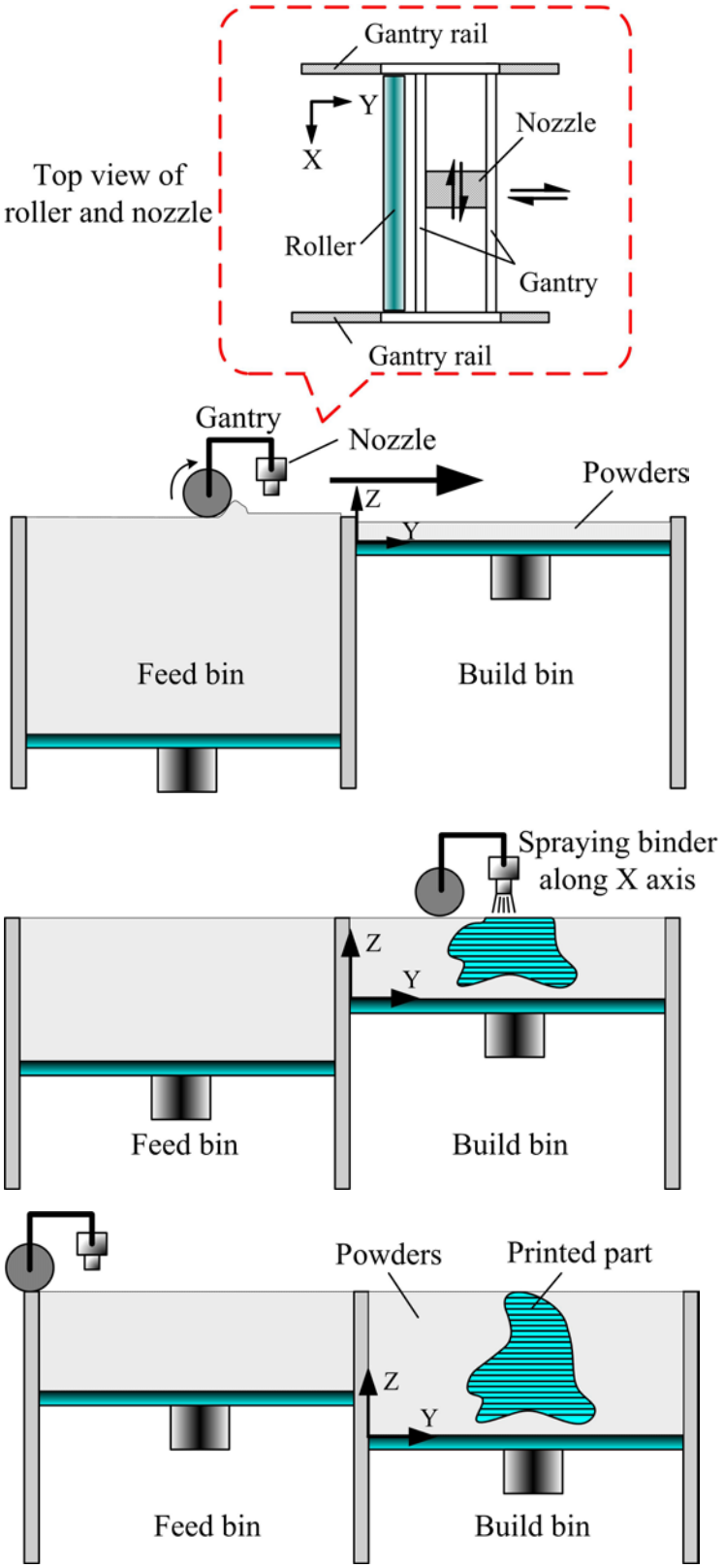

Fig. 2. Schematic 3DP process: (a) Preparation for printing, (b) During printing and (c) End of printing

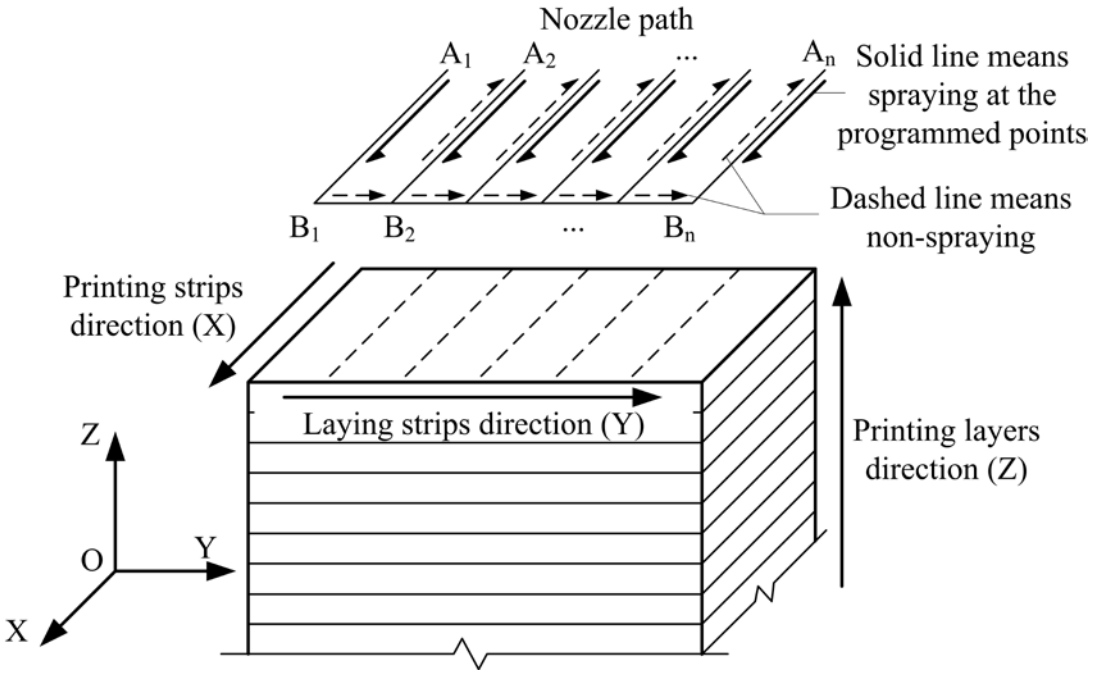

Fig. 3. Directional description of 3DP process

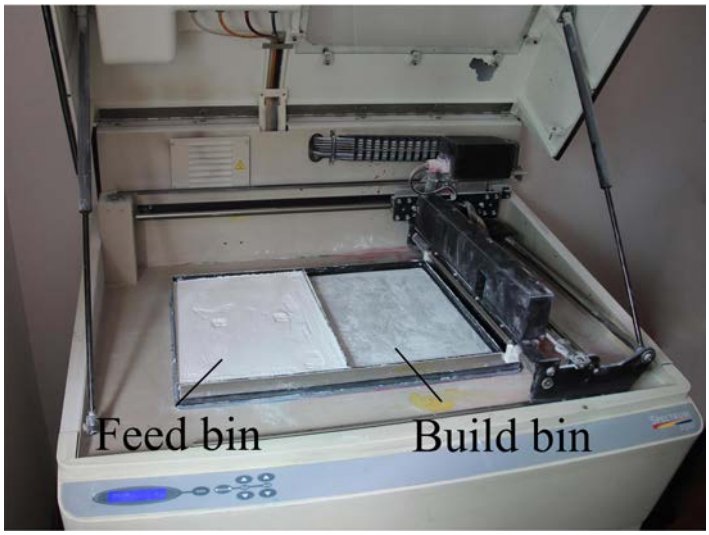
Feed bin
Build bin

Fig. 4. Printing procedure of 3D printer Spectrum Z510: (a) Preparation of powder bed, (b) During printing, (c) Removal of printed components and (d) Curing in oven

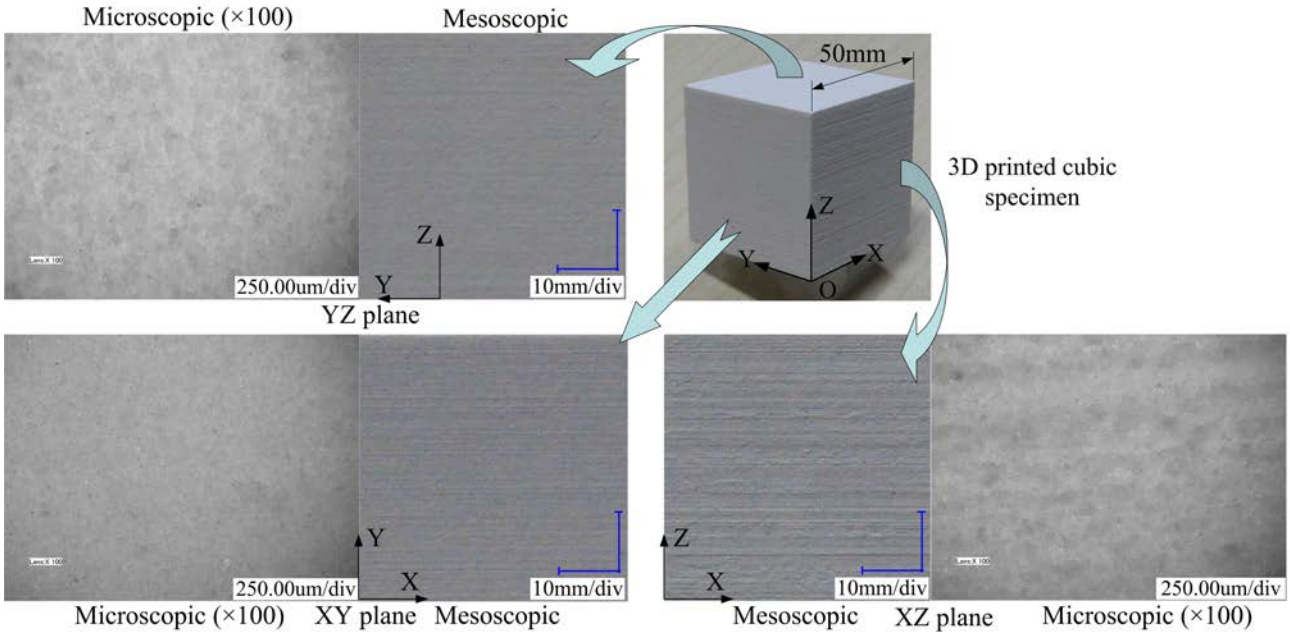

Fig. 5. Surface structure of a 3D printed cube

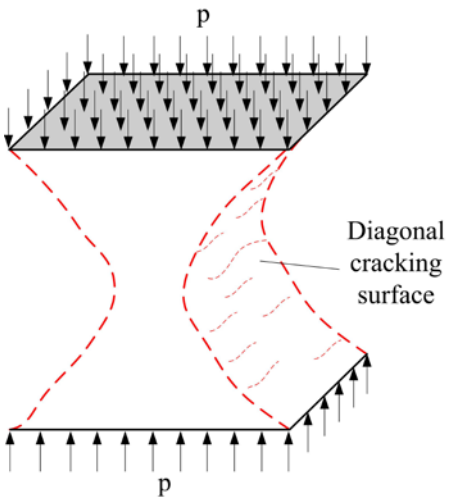

Fig. 6. Sketch of failure mode of cubic specimens under compression

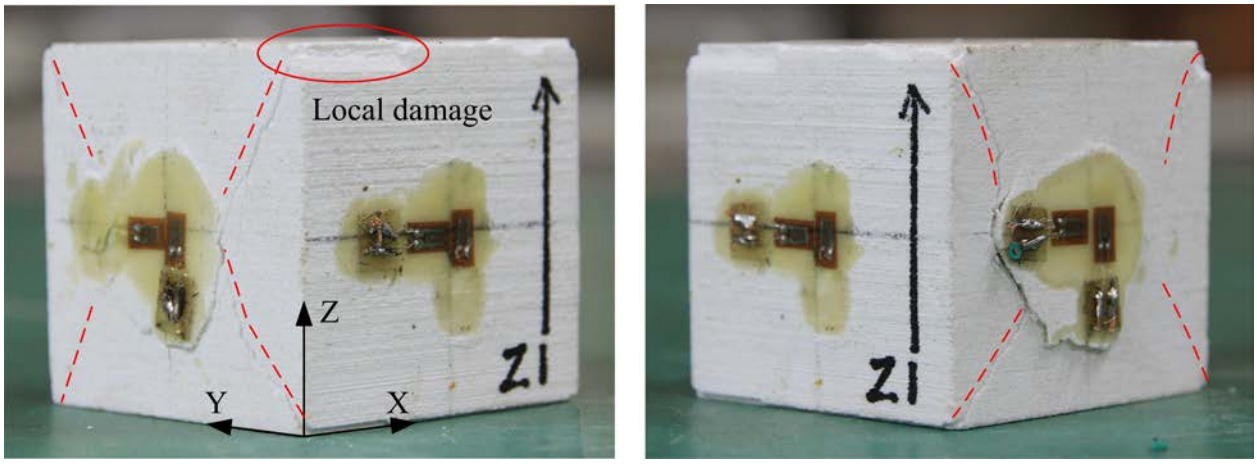

Fig. 7 Failure of a typical cubic specimen under compression in the Z direction

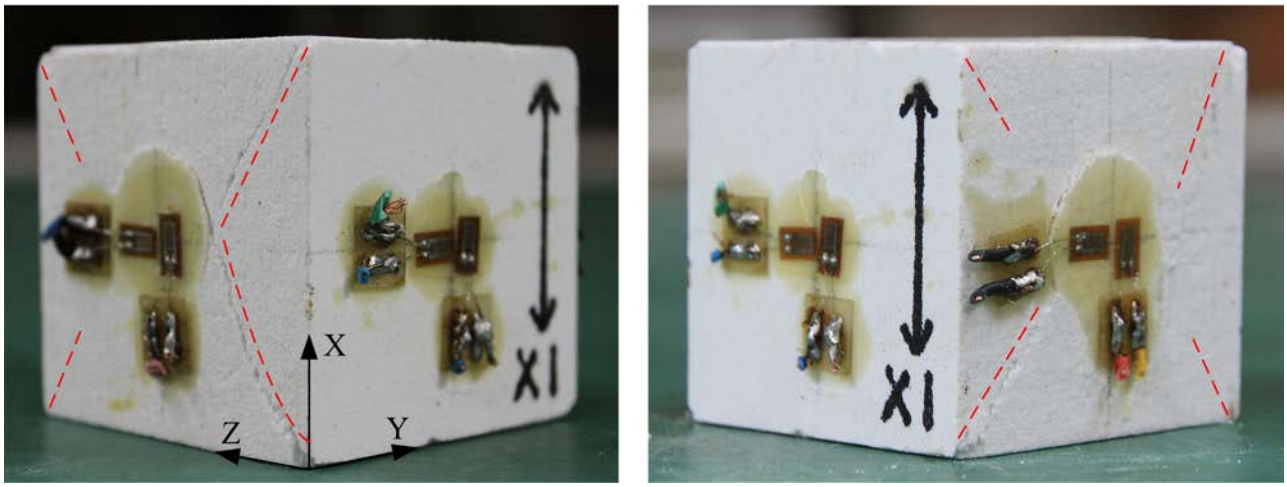

Fig. 8 Failure of a typical cubic specimen under compression in the X direction

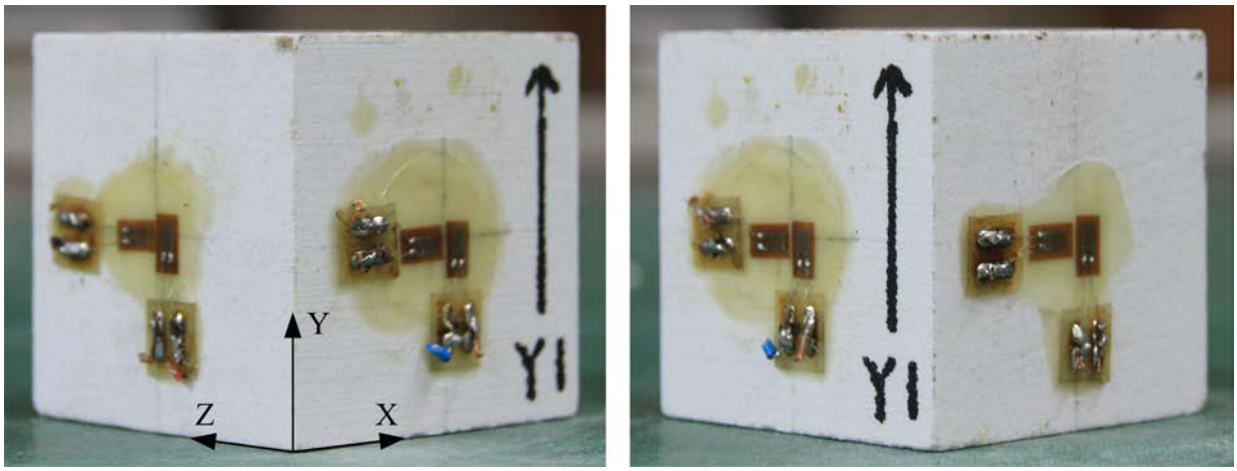

Fig. 9 Failure of a typical cubic specimen under compression in the Y direction

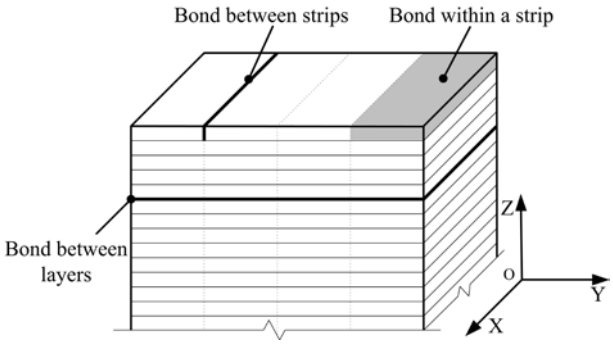

Fig. 10 Structure of a 3D printed cubic specimen

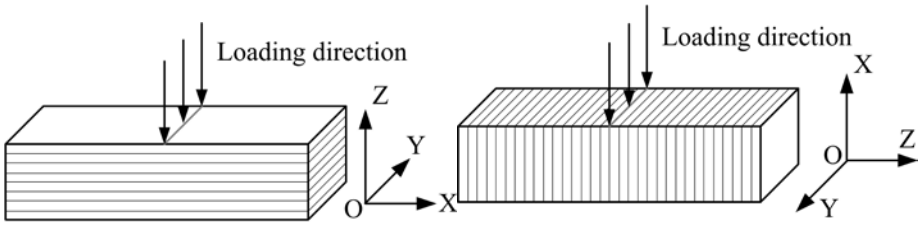

Fig.11 Loading direction of flexural specimens: (a) BZ loading and (b) BX loading

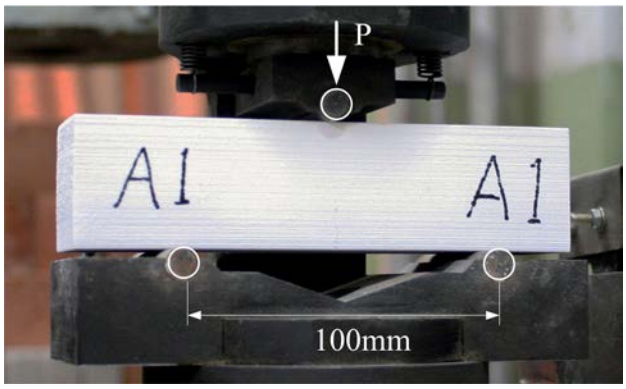

Fig. 12 Test setup of the flexural test

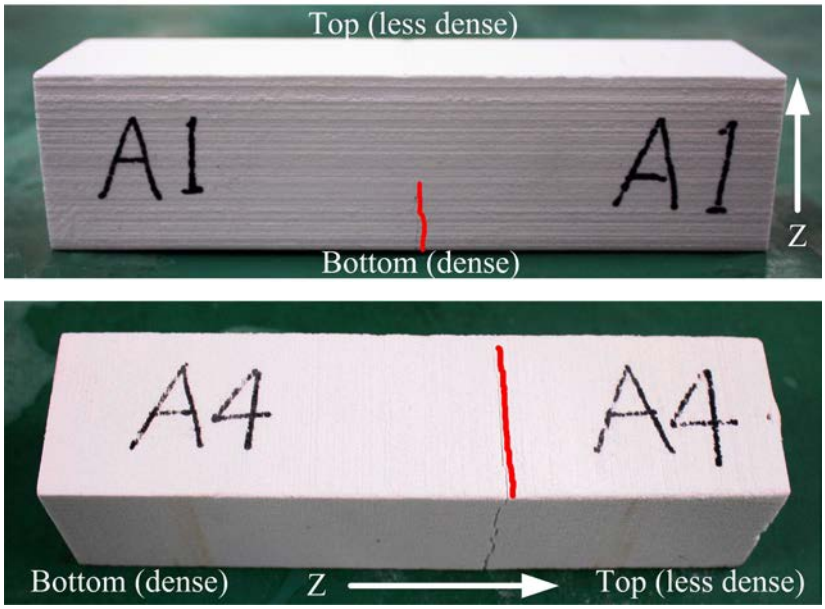

Fig. 13 Flexural failure of specimens when (a) loaded in Z direction and (b) loaded in X direction

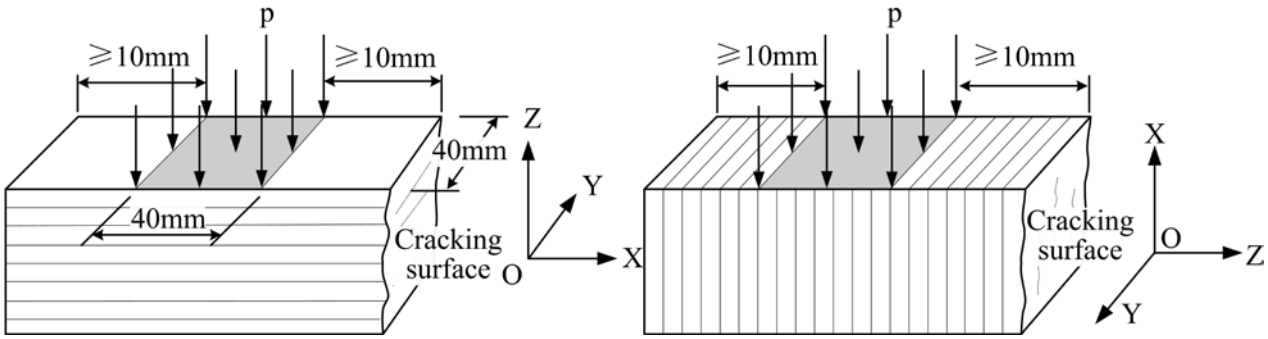

Fig. 14 Loading direction of half beams: (a) CZ loading and (b) CX loading

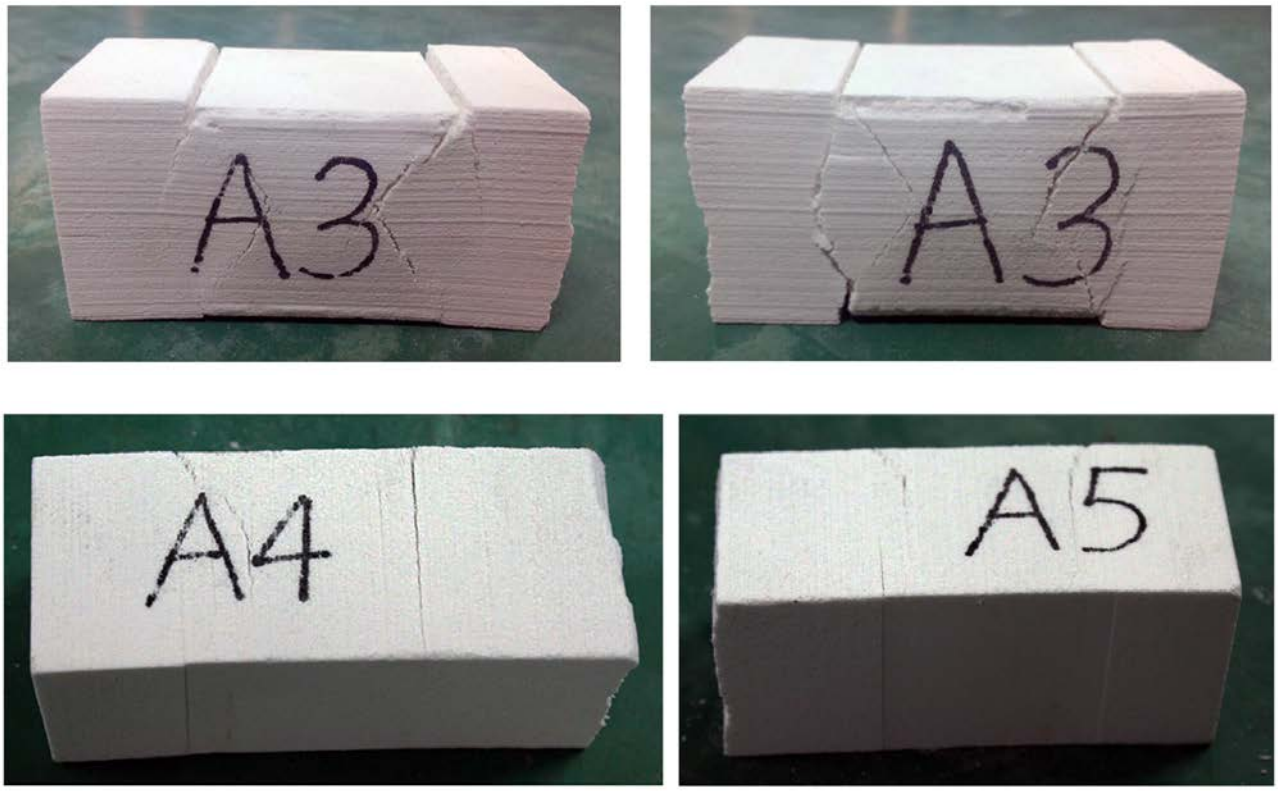

Fig. 15 Failure mode of half beam tested under compression:(a) loaded in Z direction and (b) loaded in X direction

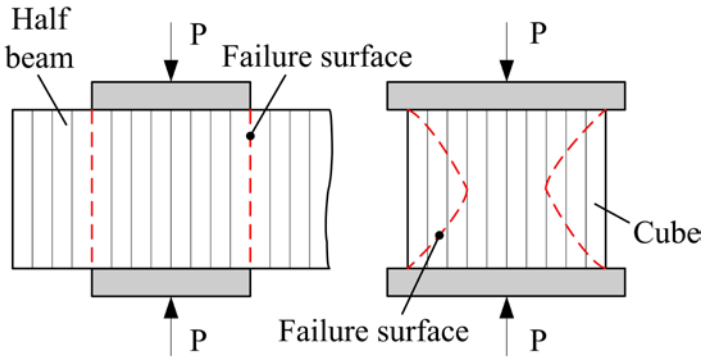

Fig. 16 Comparison of different loading methods

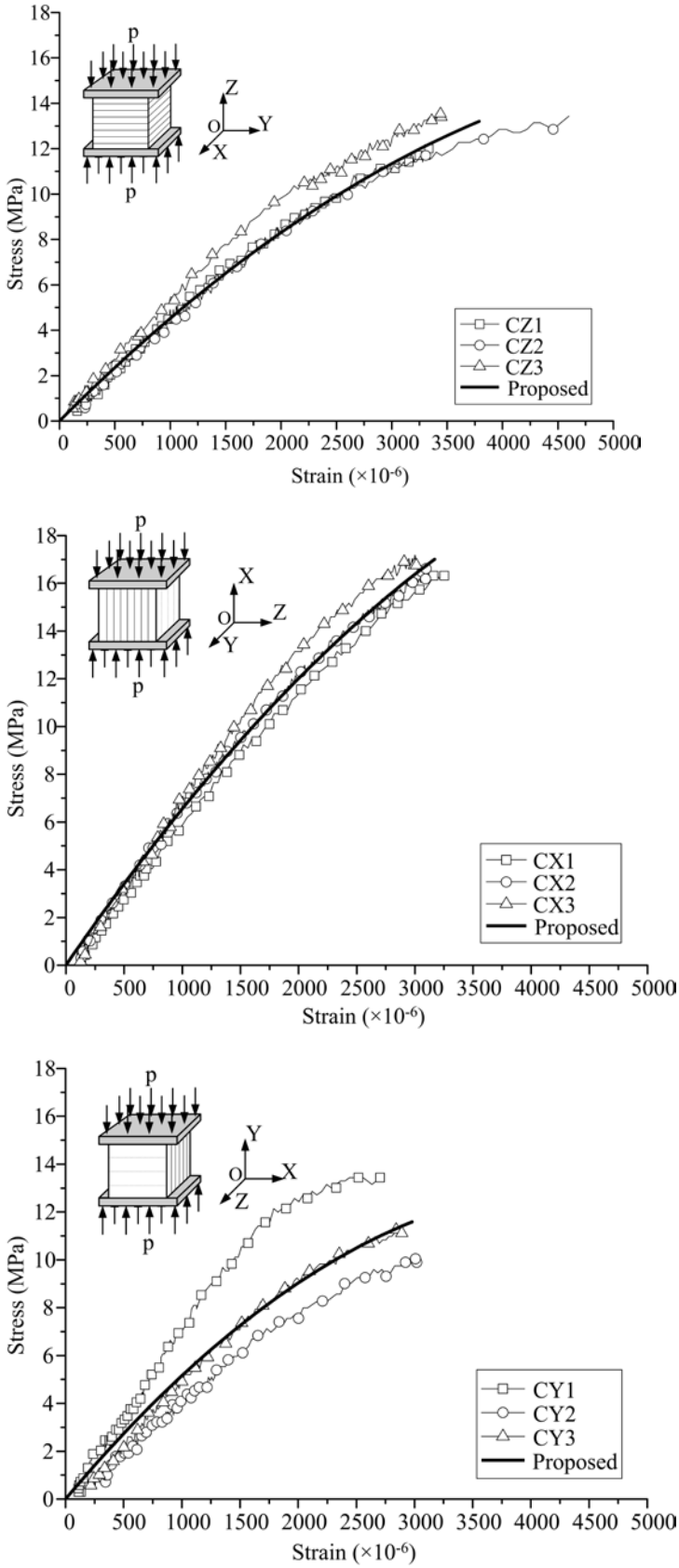

Fig. 17 The proposed uniaxial stress-strain curve vs test results: (a) loaded in the Z direction, (b) loaded in the X direction and (c) loaded in the Y direction.

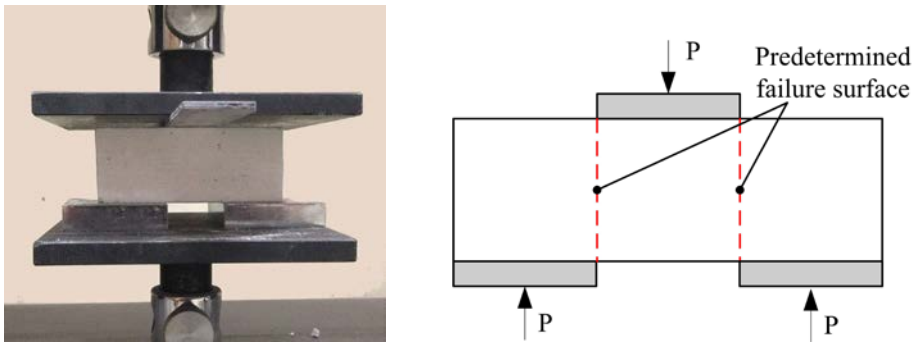

Fig. 18 Direct double shear test setup and instrumentation: (a) Photograph of specimen and (b) schematic view.

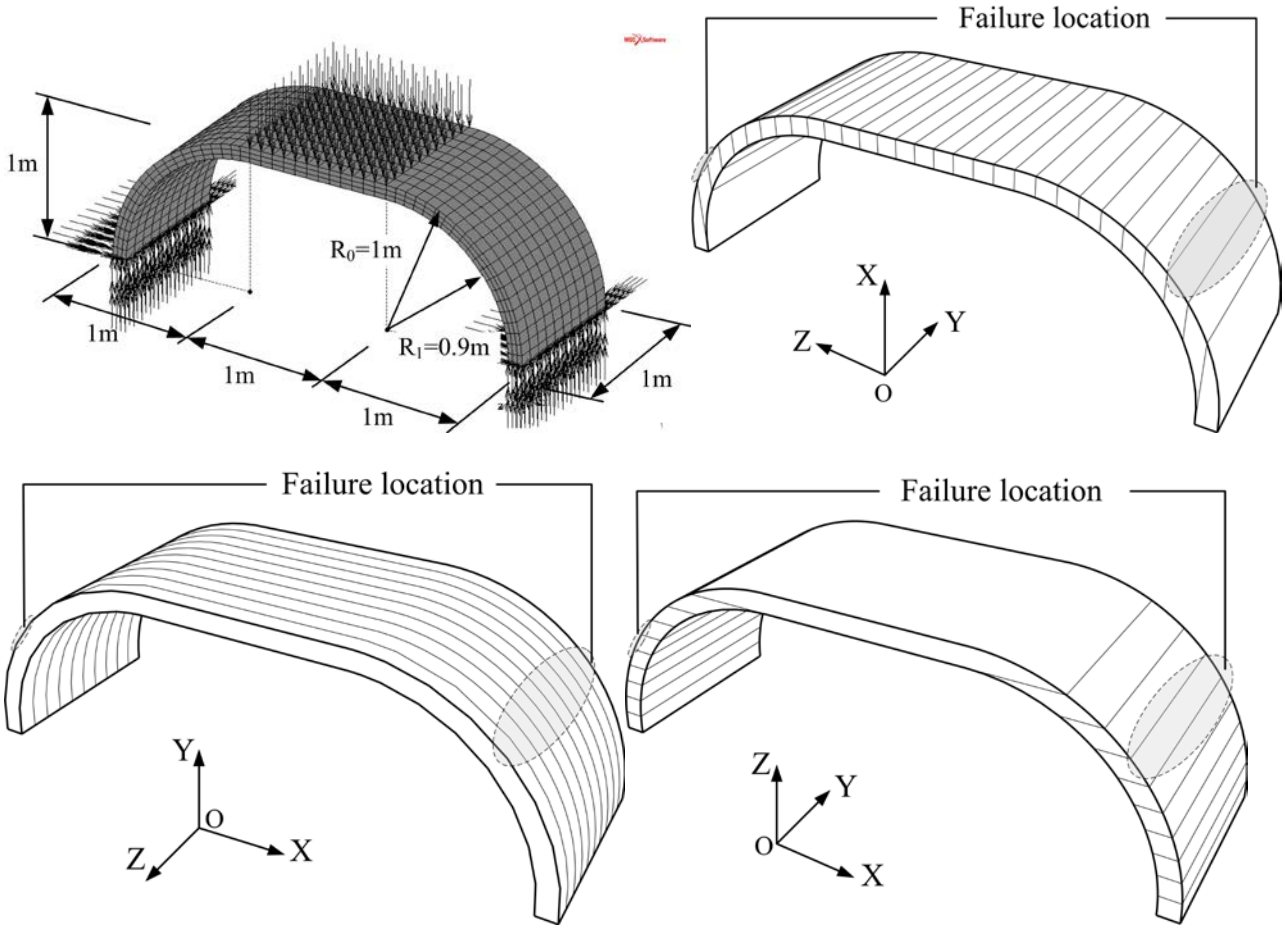

Fig. 19 Finite element models and different loading direction: (a) boundary conditions and loading, (b) loaded in X direction and failure position, (c) loaded in Y direction and failure position and (d) loaded in Z direction and failure position.

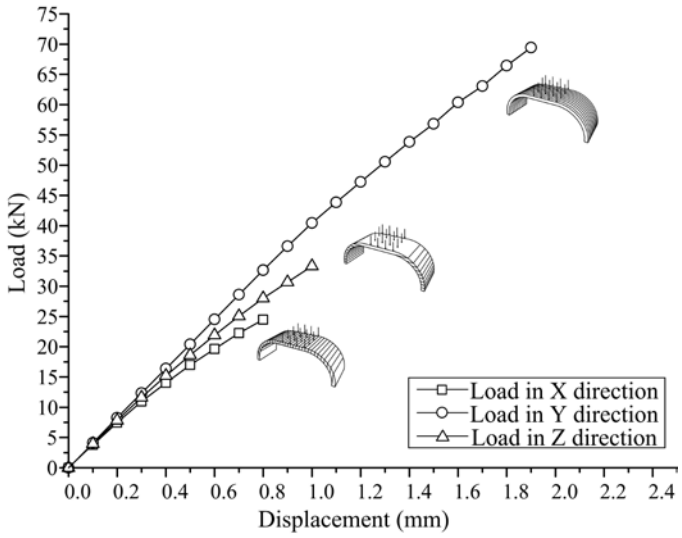

Fig. 20 Load-displacement curves of the structure when constructed in different directions